Acta Materialia 265 (2024) 119646

Contents lists available at ScienceDirect

Acta Materialia

journal homepage: www.elsevier.com/locate/actamat

Suppression of anti-phase boundary defects in Mn-Al-Ti permanent magnets

Thomas Keller [a,*], Dylan Barbagallo [a], Tushar Kanti Ghosh [b], Natalya Sheremetyeva [a], Geoffroy Hautier [a], Ian Baker [a]

[a] Thayer School of Engineering, Dartmouth College, 15 Engineering Drive, Hanover, NH 03755-8000, USA
[b] Université Catholique de Louvain, 1 Place de l'Université, Louvain-la-Neuve B-1348, Belgium

A R T I C L E I N F O

Keywords:
Mn-Al-Ti
Permanent magnet
Density functional theory
Electron backscatter diffraction
Anti-phase boundaries
Twins

A B S T R A C T

Permanent magnets (PMs) based on manganese show significant potential for applications in electric motors and devices as an alternative to Rare-earth PMs (REPMs). The metastable ferromagnetic τ phase of the Mn-Al system has magnetic performance between the REPM Nd-Fe-B magnets and the lower performance ferrite magnets. However, the maximum performance in Mn-Al PMs has not reached its theoretical limit, in part due to challenges in controlling crystalline defects such as anti-phase boundaries (APBs). APBs act as nucleation sites for domain reversal in Mn-Al and negatively affect magnetization by interrupting the $L1_0$ ordering, placing Mn atoms into AFM-coupled Mn-Mn configurations. In this study, *Ab-initio* modeling was used to screen ternary elements based on their affinity to segregate to the APB and on their preference for FM configuration. The ternary element addition of 1 at.% Ti lowered the density of APBs as observed in a transmission electron microscope. The 1 at.% Ti addition was observed to improve $(BH)_{max}$ over the base alloy, by preserving H_{ci} and improving M_r. It also significantly increased the fraction of twin boundaries in the τ phase. AFM behavior that was observed in the base alloy during T_C heating experiments (Néel behavior) and high-field VSM measurements (spin-flop behavior) was effectively suppressed with the addition of Ti. Additionally, the Ti addition thermally stabilized H_{ci} at 550 °C, improving τ phase processability. Other candidate elements, Cr, V, and Zr, were modeled to have similar potential for minimizing APBs when added to Mn-Al.

1. Introduction

The ferromagnetic τ phase in the Mn-Al system is a promising candidate for permanent magnet (PM) applications to fill the gap between high-performance rare-earth (RE) magnets and lower performance ferrite magnets. The tetragonal ($L1_0$) structure of the τ phase has a desirable combination of saturation magnetization, $M_s \sim 161$ Am^2/kg, magnetocrystalline anisotropy energy (1.5 MJ/m^3), and, thus, coercivity, H_{ci}, depending on its microstructure, giving it a maximum energy product, $(BH)_{max}$ of ~100 kJ/m^3 [1]. However, the progress to produce Mn-Al PMs of $(BH)_{max}$ comparable to the theoretical maximum has been obstructed by the metastable nature of the τ phase and the formation of defects, such as twins and anti-phase boundaries (APBs), during the phase transformation to τ phase. The τ phase is formed from the high-temperature ε phase by a hybrid displacive-diffusional phase transformation involving an intermediate ordered ε' phase. The transformation can proceed by either annealing the ε phase at ~450 °C or by cooling from the ε phase at a rate of 3.5–10 °C/s from >850 °C [2,3]. The displacive mode (ε ordering to ε' followed by shear to τ) is observed to be kinetically dominant at <450 °C whereas the diffusional mode (compositionally invariant massive transformation from ε to τ) is kinetically dominant at >450 °C. However, both transformation modes are believed to always occur simultaneously in varying proportions of dominance [4–9]. The displacive transformation mode is also made dominant by alloying with C or increasing the Mn content, whereas a higher Al content will favor the diffusional mode [10]. The hybrid displacive-diffusional phase transformation commonly produces twins, APBs, and stacking faults in the τ phase.

Unfortunately, APBs diminish $(BH)_{max}$ in two primary ways. First, the APB acts as a nucleation site for reversing domains, thereby diminishing H_{ci} and M_r [11,12]. Second, the APB pairs Mn atoms across the boundary as anti-site defects that prefer AFM-coupling, thereby reducing M_r and M_s [13] Therefore, it is beneficial to identify factors that reduce the formation and magnetic effects of APBs. This defect is a disruption of the binary $L1_0$ ordering of Mn and Al. It has been observed that APBs are a result of ½[101] lattice shearing during the hybrid

---

* Corresponding author.
E-mail address: Thomas.robert.keller@dartmouth.edu (T. Keller).

https://doi.org/10.1016/j.actamat.2023.119646
Received 19 October 2023; Received in revised form 21 December 2023; Accepted 30 December 2023

displacive-diffusional phase transformation from the high-temperature ε phase [12,14]. Néel-type AFM behavior has been observed in Mn-Al during Curie temperature (T_C) measurements, shown as increasing M with temperature (Néel) rather than the typical loss of M with temperature (Curie) due to thermal perturbation, see Fig. 1 [15–19]. The geometry of an APB is shown in Fig. 2. A noticeable increase in M has been observed at temperatures as low as 100 °C and persists even in alloys annealed for 16 h at 550 °C, making it improbable that the increase in magnetic moment is due to increased ordering of the $L1_0$ τ phase during the T_C measurement. Additionally, the Néel temperature, T_N, of the AFM ε phase is ~−180 °C, compared to the τ phase at ~300 °C, thus untransformed parent ε phase left over from the phase transformation to τ could likewise not explain the Néel-type behavior [20,21].

On the other hand, twins have a less clear impact on the magnetic properties of Mn-Al. While several studies have claimed a negative effect of twins on M_r and H_{ci} they have not separated the effects of twins from the effects of APBs [22–24]. Modeling has showed that order twins (86° disorientation angle) have a lower nucleation field and higher pinning field for reversing magnetic domains compared to true twins (76° disorientation angle), making order twins more likely to negatively affect H_{ci} than true twins [12]. However, the negative effect of twins on H_{ci} claimed by Thielsch et al. and Jia et al. rely on observations made using Kerr and Lorentz microscopy on regions containing a high density of twins but without quantification of the density of APBs within the region [23,25]. This neglects to test the likely situation that methods that improve magnetic properties by suppressing twins also remove or suppress APBs. In fact, the few studies that have simultaneously compared the effects of twins and APBs on magnetic properties claim that twins act as pinning sites (improve H_{ci}) while APBs act primarily as nucleation sites (lower H_{ci}) for magnetic domain reversal [26–28]. Therefore, the only consensus in the literature is that APBs have a negative effect on H_{ci}. Twins, on the other hand, are correlated with lowered M_r and H_{ci} but may not actually be the causal element. It is worth noting that the TEM study by Landuyt and Tendeloo [26] characterized the highest performance Mn-Al PM ever produced (55.7 kJ/m^3) and found a high density of twins but no APBs in the hot-extruded PM.

In addition to controlling defects, the thermal stability of M_r, and H_{ci} is particularly important for processing Mn-Al into commercially viable PMs. The conventional PM processing technique is to mill the FM powder to a fine grain size and high dislocation density (high H_{ci}), align in a magnetic field (high M_r), then sinter into a high density bulk PM at elevated temperature (high $(BH)_{\max}$). However, due to the metastable nature of the τ phase, it is common for H_{ci} and M_r to be reduced due to defects annealing out, grain coarsening, or phase decomposition during any of these steps [1,29,30]. This is also applicable to recent, more advanced PM processing techniques, such as additive manufacturing [31].Therefore, any inherent improvement to the thermal stability of H_{ci} or M_r by a ternary alloyant will greatly improve the real-world processability of the τ phase.

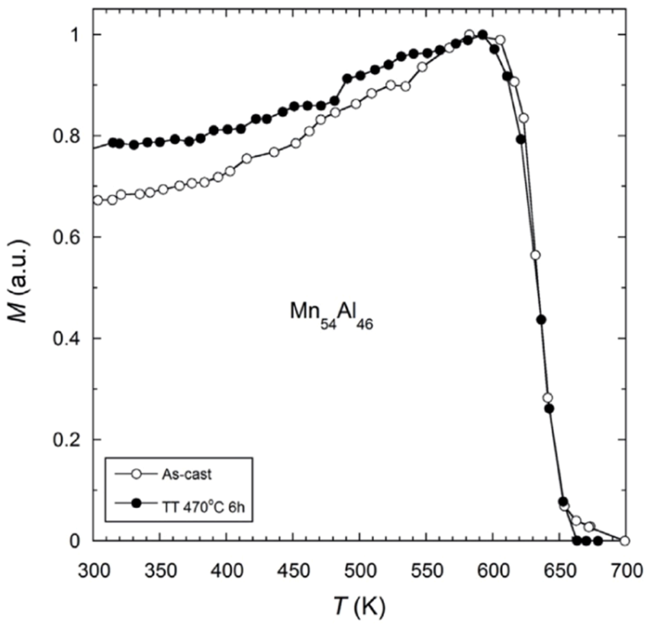

Fig. 1. Thermal VSM measurement of $Mn_{54}Al_{46}$ τ phase exhibiting AFM behavior of increasing M with increasing T up to T_C. From [19].

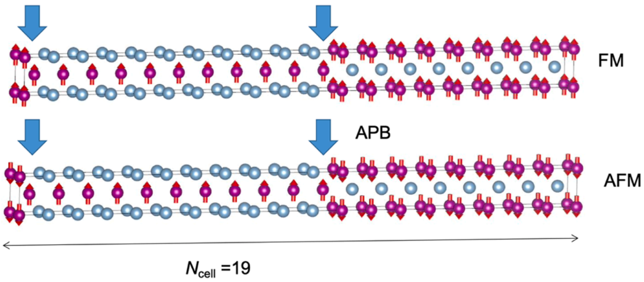

Fig. 2. Schematic showing the DFT supercell used to model the effects of elemental substitution on the APB. Mn atoms shown with their magnetic moment spin as an arrow and Al atoms shown without. The large arrows indicate the locations of two APBs in the supercell.

This study uses *Ab-initio* modeling as a tool to rapidly screen elements for their ability to suppress APBs by two main characteristics: a) an element's affinity to segregate to the APB rather than sit in the bulk, and b) an element's tendency to promote FM coupling across the APB compared to AFM-coupling. This study identifies Ti addition as an effective method to reduce the APB density in Mn-Al and improve the thermal stability of the τ phase. It also identifies other effects from Ti addition on the microstructure and shows how these microstructural changes positively benefit the magnetic properties. Ti has previously been tested as a ternary alloyant in $Mn_{54}Al_{46}$ substituting 2 at.% and 4 at.% for Mn. However, these compositions resulted in 35 wt.% to 75 wt.% τ phase, with a remainder fraction of γ_2 phase in $Mn_{52}Al_{46}Ti_2$ and a remainder fraction of a mix of γ_2 phase and a soft magnetic κ phase (prototype CsCl) in $Mn_{50}Al_{46}Ti_4$ [32]. The κ phase has also been observed in Mn-Al-Ni alloys and, due to its lower values magnetocrystalline anisotropy, T_C, and M_s, it does not improve the magnetic properties of the τ phase and should be avoided. Therefore, this study focused on lower concentrations of Ti (≤2 at.%) to avoid κ phase formation.

2. Experimental

Alloys of composition $Mn_{54}Al_{45}Ti_1$ and $Mn_{53}Al_{46}Ti_1$ were cast using arc-melting under an Ar atmosphere. The cast buttons were flipped 3 times to ensure homogeneity. Excess (6 wt.% Mn) was added to each alloy to achieve the desired composition due to the higher vapor pressure of Mn relative to Al and Ti. A reference $Mn_{54}Al_{46}$ alloy was prepared via induction melting by Sophisticated Alloys, Inc. Alloy composition and homogeneous distribution of Ti was confirmed via electron dispersive spectroscopy (EDS) in a Tescan Vega3 scanning electron microscope (SEM). Differential scanning calorimetry (DSC) was performed in a TA instruments Q20 from 30 to 600 °C under flowing Ar at ramp rates of 5–80 °C/min. The ε phase of each alloy was prepared by annealing at 1100 °C for 70 min in a sealed alumina tube followed by quenching into deionized water. The tube was evacuated to −85 kPa and backfilled with Ar gas to 15 kPa to minimize oxidation. The ε phase was transformed to τ at the temperature identified via DSC for a duration where magnetization and coercivity were both optimized. For $Mn_{54}Al_{46}$ this was 450 °C for 30 min and for both $Mn_{54}Al_{45}Ti_1$ and $Mn_{53}Al_{46}Ti_1$

this was 550 °C for 60 min. Transmission electron microscopy (TEM) was performed in an FEI Tecnai F20ST FEG TEM at 200 kV to analyze the twins and APBs. Electron backscatter diffraction (EBSD) was done in a Thermo Fisher Helios 5 SEM to characterize grain size, orientation, texture, dislocation density, and for phase identification. TEM sample preparation utilized focused ion beam (FIB) milling in the Helios 5 SEM. X-ray diffraction in a Rigaku UltraX XRD with a Cu-anode ($\lambda = 0.154$ nm) was used to identify the phase volume fractions and lattice parameters. T_C and hysteresis curves were measured in a Lakeshore 7300 vibrating sample magnetometer (VSM) equipped with a high temperature furnace. High-field VSM was performed in a 9 T Quantum Design PPMS Dynacool with VSM. Room temperature VSM was demagnetization corrected based on rectangular prism sample geometry using the model from [33]. Thermal stability studies were performed at 250 °C (for 40 days) and 550 °C (for 1 week) by progressively annealing samples in air and performing VSM measurements at fixed intervals.

3. Calculations

Ab-initio modeling was used to model the effects of different ternary element additions to the τ phase. In keeping with previous modeling by Keller et al. [34], spin-polarized calculations were made with density functional theory (DFT) in the Vienna *Ab-initio* Simulation Package (VASP) using the projector augmented wave (PAW) method and the generalized gradient approximation with the Perdew-Burke-Ernzerhof (GGA PBE) exchange-correlation functionals [35–38]. Details of these calculations are described in [34]. To model the APB behavior in the τ phase, the same DFT VASP code was used. The initial unit cell state for the τ phase was calculated with PAW PBE 5.4, an energy cutoff equal to 450 eV, and a Monkhorst-Pack k-point grid of 23 × 23 × 17 of the Brillouin zone. A $Mn_{20}Al_{18}$ APB model of 19 cells and 38 atoms was chosen in accordance with previous APB modeling by Nieves et al. [11,39].

To evaluate the tendency for the ternary element to segregate to the APB compared to the bulk, the energy of formation was calculated for the APB defect, comparing substitution on the Mn site (shown as gold in the box in Fig. 3) with substitution to the bulk (at the "D" site shown in Fig. 3) as follows:

$$E^F[Z] = E^{tot}[APB] - E^{tot}[bulk] - (-1)\mu^{Mn} - (1)\mu^Z \quad (1)$$

where E^F is the energy of formation of the APB when substituting the ternary element, Z, for Mn at the APB, E^{tot} is the total energy for the ternary element at a given location (at the APB or in the bulk), and μ is the chemical potential for Mn or Z. Therefore, if $E^F[Z]$ is negative, the APB is favored to form in the presence of Z and the substitutional atom is therefore favored to segregate to the APB compared to the bulk, as desired [40]. The next part of the screening process compared the FM versus AFM energies with the ternary element substituted for Mn on the APB. The AFM APB's energy was compared to the FM APB's energy with the substitutional atom on the Mn site of the APB in both cases, and the difference in energy was calculated.

The Kissinger method was used to determine activation energies from DSC measurements. The Kissinger (Eq. (2)) [41] method is based on an Arrhenius model of reaction rates, as described in [42,43]:

$$\ln\left(\beta/T_{\max}^2\right) = \left\{\ln(AR/E_a) + \ln\left[n(1-\alpha)^{n-1}\right]\right\}E_a/RT_{\max} \quad (2)$$

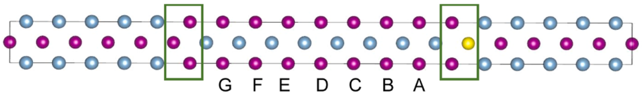

Fig. 3. Schematic showing the Mn substitutional site as a gold atom in the box marking the APB. The energy of formation approaches the bulk as the substitutional atom moves from the APB to site D.

where β is the heating rate, T_{max} is the exotherm peak temperature, A is the Arrhenius factor, R is the molar gas constant, E_a is the activation energy, n is the reaction order, and α is the fraction transformed. DSC curves at β values of 5–80 °C/min yielded a plot of $\ln(\beta/T_{max}^2)$ against $-1/T_{max}$. The slope of the ordinary least squares (OLS) regression line (E_a/R) was used to calculate E_a.

4. Results

4.1. Ab-initio modeling

Candidate ternary elements were screened using DFT to understand how they interacted with an APB. The $Mn_{50}Al_{50}$ $L1_0$ τ phase structure was relaxed to the lattice parameters $a = 2.755$ Å, $c = 3.471$ Å, in good agreement with the experimental parameters in Table 3. This ground state had an average magnetization along the magnetically-easy c-axis of $\mu_{Mn} = 2.264\mu_B$ per Mn atom, $\mu_{Al} = -0.050\mu_B$ per Al atom and a total average magnetization of $1.107\mu_B$ per atom in the $Mn_{50}Al_{50}$ functional unit [34]. The supercell of $Mn_{20}Al_{18}$ used to model the APB, which is shown in Figs. 2 and 3, contains two APBs due to the periodic boundary conditions of the model. At the APB interface the magnetic moments of the Mn atoms are shown as collinear along the c-axis, in the FM (spins aligned) and AFM (spins opposed) configurations.

Fig. 4 shows that, of the candidate elements studied, all except Fe, Co, Ni, and Cu favor segregating to the APB. 54-atom supercells of the fully ordered τ phase were relaxed with DFT to understand the preferred location of the Ti atom in the absence of an APB defect. By performing a parallel calculation to Eq. (1), the Ti substitutional defect formation energy for $Mn_{26}Al_{27}Ti_1$ (Ti on Mn site) was 0.353 eV and the defect formation energy for $Mn_{27}Al_{26}Ti_1$ (Ti on Al site) was −0.063 eV. This indicates that the Ti atom prefers the Al site in the bulk τ phase.

The energy difference between AFM and FM APB configurations are shown in Fig. 5. The more negative the energy difference for an element, the more stable the AFM configuration is at the APB compared to the FM configuration. All the candidate elements, except Ni, were shown to stabilize the FM configuration compared to the Mn baseline, as desired, but Fe, Co, and Cu were eliminated given their preference for the bulk rather than segregating to the APB.

4.2. Phase transformation

DSC measurements are shown in Fig. 6 and Table 1 of quenched ε phase samples heated at a constant rate to transform to the τ phase. The peak of the ε' phase ordering transformation was changed by <10 °C with the addition of Ti. However, the peak of the hybrid transformation to τ phase was increased by 39 °C in $Mn_{53}Al_{46}Ti_1$ and increased by 56 °C in $Mn_{54}Al_{45}Ti_1$. The Mn-Al-Ti alloys also had a lower calculated activation energy to transform to the ε' phase, but a higher activation energy to transform to the τ phase.

Fig. 7 shows the results of annealing the three alloys at 450 °C and 550 °C from the ε phase to the τ phase. In good agreement with the DSC results, the ε phase $Mn_{54}Al_{46}$ alloy readily transformed to the τ phase at 450 °C with optimum properties at 30 min. Likewise, the Mn-Al-Ti alloys had a slower transformation to the τ phase and required a 550 °C heat treatment for 60 min to achieve the same mix of high magnetization (indicative of the τ phase fraction) with high coercivity achieved for $Mn_{54}Al_{46}$ at 450 °C. Optimized magnetic properties were chosen to best compare the three alloys at similar levels of transformed τ phase, defect density, and grain size and minimize extrinsic variables. Although it would have been ideal, it was not possible to perform the same heat treatment on all three alloys without under-transforming the Ti alloys or over-coarsening the Mn-Al alloy.

4.3. Microstructure

TEM was performed to characterize the APB density in the three

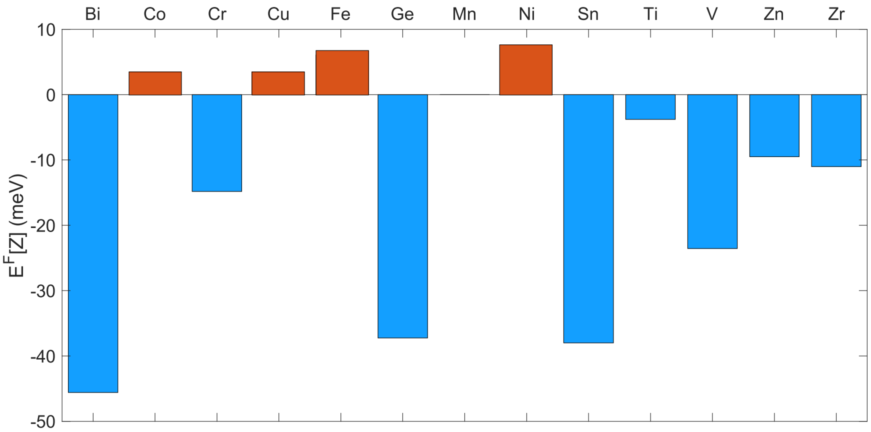

Fig. 4. DFT results for the energy of formation of the APB with the 12 ternary elements located at the APB. The more negative $E^F[Z]$, the more favorable it is for the element to segregate to the APB.

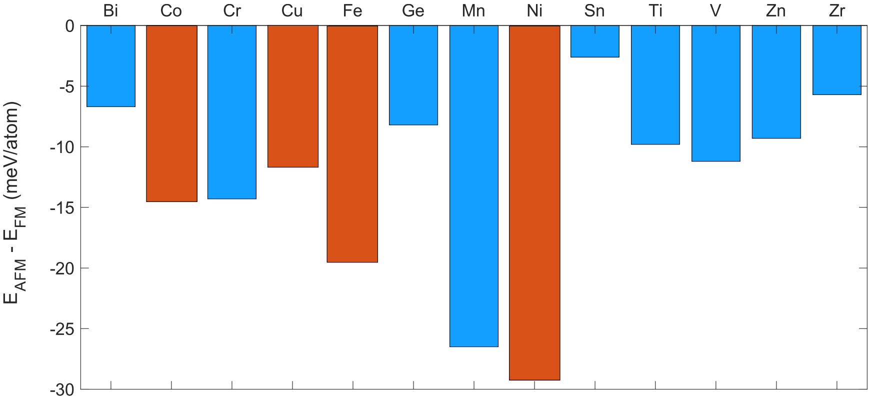

Fig. 5. DFT results for the difference in energy of an AFM configuration compared to an FM configuration at the APB for a given ternary element. The elements in red do not favor the APB compared to the bulk as shown in Fig. 4.

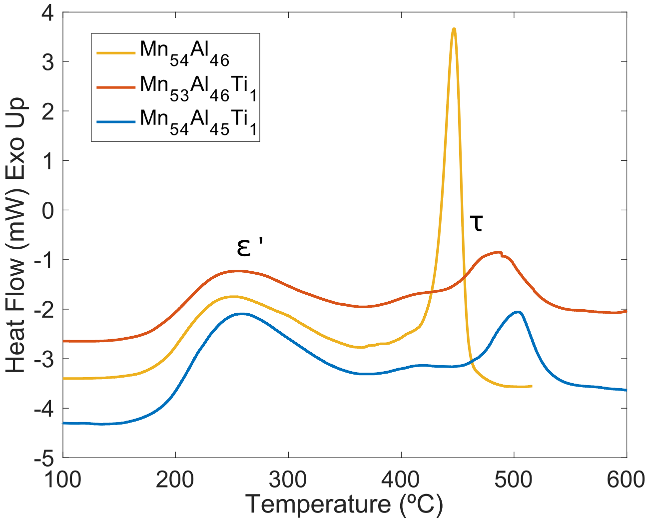

Fig. 6. DSC heat flow as a function of temperature at a heating rate of 10 °C/min. The low-temperature exotherm is the ordering of ε phase to ε' and the high-temperature exotherm is the transformation to τ phase.

Table 1
The phase transformation peak temperatures, activation energy, and enthalpy calculated for the Mn-Al-Ti alloys from DSC measurements.

Property	$Mn_{54}Al_{46}$	$Mn_{53}Al_{46}Ti_1$	$Mn_{54}Al_{45}Ti_1$
ε' phase peak °C (10 °C/min)	252	256	259
τ phase peak °C (10 °C/min)	447	486	503
ε' E_a kJ/mol (f.u.*)	142 ± 13	112 ± 8	81 ± 9
ε' ΔH J/g	44 ± 8	31 ± 6	32 ± 7
τ E_a kJ/mol (f.u.*)	155 ± 8	168 ± 13	196 ± 19
τ ΔH J/g	40 ± 6	28 ± 7	27 ± 6

* Note: the g/mol of the different formula units for the three compositions are all within 0.5 % and do not affect the E_a values by more than the significant figures given.

alloys to determine if Ti had a clear effect on APB density, see Fig. 8. Bright-field (BF) and centered dark-field (CDF) using a selective area diffraction (SAD) aperture were used to image APBs present in the samples. The invisibility criterion for a crystal defect in TEM is met when α, the phase factor, is equal to $2\pi n$, where n is an integer. Given a diffraction vector, $\vec{g}$ and a defect fault vector, $\vec{R}$, the invisibility criterion is met when $\alpha = 2\pi \vec{g} * \vec{R} = 2\pi n$ [44,45]. Because APBs in Mn-Al have the fault vector, $\vec{R} = \pm\frac{1}{2}<101>$, they will all therefore be visible in CDF using any superlattice spot and invisible when using a fundamental spot [27].

Fig. 8 clearly shows the density of APBs decreases with the addition of 1 at.% Ti, as desired, shown by the APBs visible in the DF images. APBs were only visible in the presence of twins in the three alloys, and the twins are visible as long striated bands in the BF images.

The composition of the Mn-Al-Ti alloys were confirmed via EDS as shown in Table 2, with compositions within 0.5 at.% of the target composition. The addition of 1 at.% resulted in a small lattice expansion

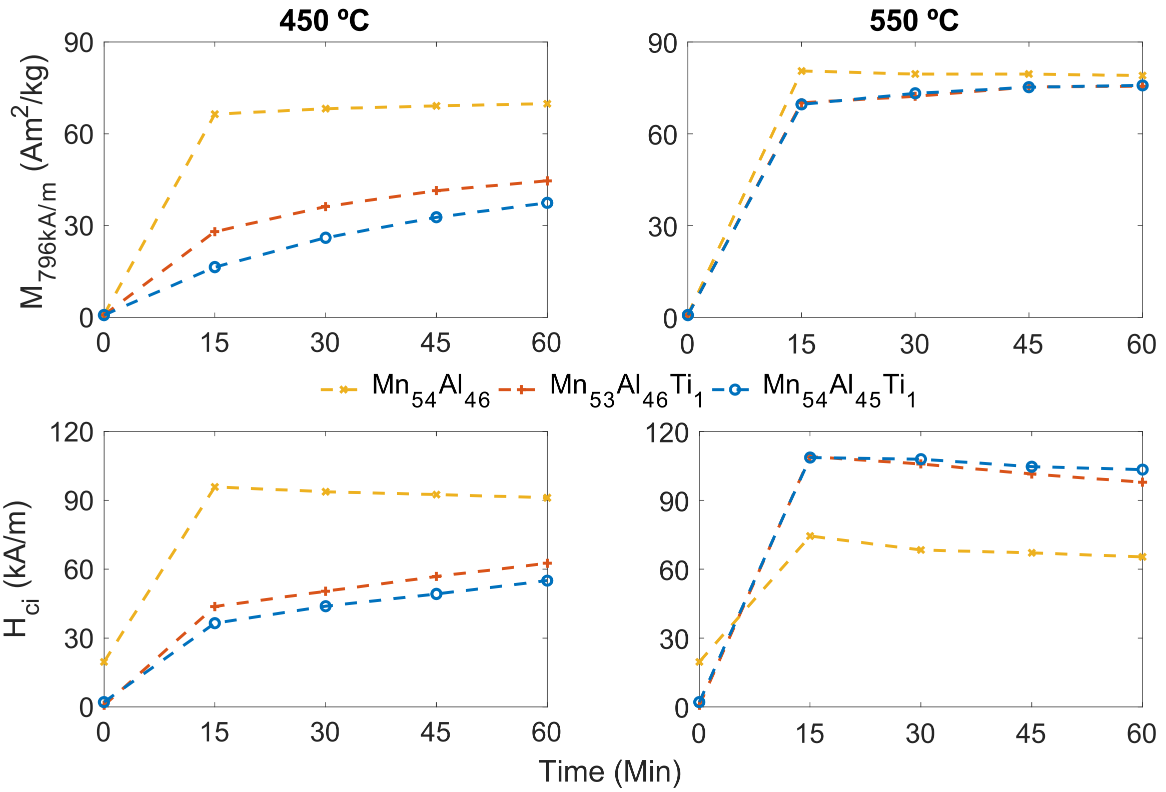

Fig. 7. The variation of $M_{796kA/m}$ and H_{ci} with respect to time for heat treatments at 450 °C and 550 °C.

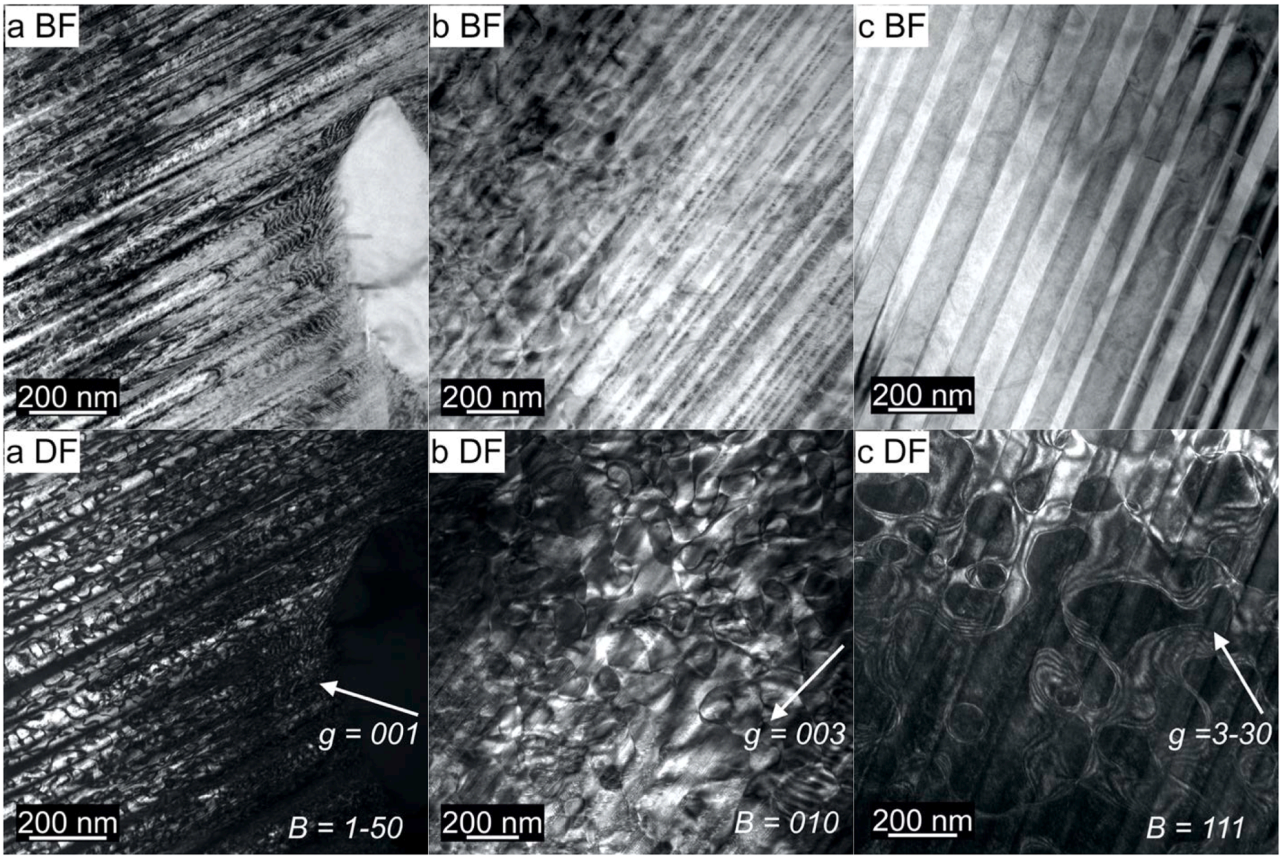

Fig. 8. TEM BF and DF images of Mn-Al-Ti alloys showing how the density of APBs decreases with Ti addition. (a) $Mn_{54}Al_{46}$ (b) $Mn_{53}Al_{46}Ti_1$ (c) $Mn_{54}Al_{45}Ti_1$. *B* is the beam direction and *g* is the diffraction vector.

Table 2
Compositions of the Mn-Al-Ti alloys measured with EDS.

Composition	$Mn_{53}Al_{46}Ti_1$	$Mn_{54}Al_{45}Ti_1$
Mn	52.5 ± 0.19	54.2 ± 0.8
Al	46.5 ± 0.2	44.7 ± 0.8
Ti	1.0 ± 0.03	1.1 ± 0.06

in both the c and a dimensions of the τ unit cell, as shown in Table 3. While increasing the volume of the unit cell has been shown to improve the magnetic moment per atom, these changes of 0.5 % are too small to be a likely source of changes to the magnetic properties [46].

The microstructure of the Mn-Al-Ti alloys was characterized using XRD and EBSD as summarized in Tables 3 and 4. True twins (76° misorientation) were significantly increased in the Mn-Al-Ti alloys. There was a negligible effect on the geometrically-necessary dislocation (GND) density and the prevalence of order twins (86° misorientation) and pseudo-twins (48° misorientation). All three compositions had a GND density of $\sim$2–3•10^{14}/m^2. Because the three alloys could not be transformed to the τ phase using an identical heat treatment, it is possible that differences in the grain size between the three alloys were influenced by coarsening rather than intrinsically related to Ti addition. The heat treatments were chosen to minimize this effect. Twins and dislocations are an inherent byproduct of the hybrid transformation to the τ phase and are not affected in the same manner, i.e. neither would increase in density due to prolonged annealing after the phase transformation is complete.

Fig. 9 shows the grain morphology between the three alloys using EBSD. Whereas the $Mn_{54}Al_{46}$ alloy is characterized by mostly small, randomly oriented grains and some large twinned grains, the Mn-Al-Ti alloys have much larger grain regions intersected by a high density of twins which appear to originate on the grain boundaries.

4.4. *Magnetic properties*

The VSM curves in Figs. 10 and 11 show the effects of 1 at.% Ti substituted for either Mn or Al in $Mn_{54}Al_{46}$ in as-annealed isotropic samples. Fig. 6 contains demagnetization-corrected data used to accurately measure M_r, H_{ci}, and $(BH)_{\max}$, whereas Fig. 7 was not demagnetization corrected but gives a high-field value approaching the true M_s. The data show that, as-annealed, the addition of Ti slightly improves H_{ci} by ~8 % for both alloys and significantly improves M_r by 13 % and 22 % for $Mn_{53}Al_{46}Ti_1$ and $Mn_{54}Al_{45}Ti_1$, respectively. Consequently, $(BH)_{\max}$ is improved by 33 % in $Mn_{54}Al_{45}Ti_1$over the base alloy. To eliminate crystal texture as a cause of the improved remanence, VSM measurements were made in 3 perpendicular orientations for each sample: the short, medium, and long axes of each rectangular prism sample, and all VSM curves were demagnetization corrected using the model in [33]. The data have been averaged for the three orientations into the values of H_{ci}, M_r, and $(BH)_{\max}$ in Table 5.

Fig. 12 shows the T_C data for the three alloys when the τ phase was heated from room temperature up to 415 °C. The addition of Ti lowers T_C from 375 °C in $Mn_{54}Al_{46}$ to 365 °C in $Mn_{53}Al_{46}Ti_1$. However, it also has a noticeable effect on the slope of the magnetization curve under heating. In the alloys with Ti, the slope is always negative, as expected following Curie FM behavior, whereas the sample without Ti has a positive slope up to near T_C, indicative of Néel AFM behavior.

Table 3
Refined lattice parameters and phase wt.% fractions of the Mn-Al-Ti alloys determined via XRD.

Property	$Mn_{54}Al_{46}$	$Mn_{53}Al_{46}Ti_1$	$Mn_{54}Al_{45}Ti_1$
a (Å)	2.7763 ± 0.0003	2.7820 ± 0.0007	2.7817 ± 0.0004
c (Å)	3.5737 ± 0.0004	3.5783 ± 0.0010	3.5771 ± 0.0006
Volume (Å^3)	27.546	27.695 (0.5 % change)	27.680 (0.5 % change)
τ phase wt.%	98.5 ± 0.9	80.4 ± 0.3	95.0 ± 1.5
γ_2 phase wt.%	1.0 ± 0.4	6.1 ± 1.0	2.5 ± 1.1
β phase wt.%	0.5 ± 0.1	13.5 ± 1.0	2.6 ± 0.3

Table 4
Relative fractions of twins, grain areas, and phase wt.% fractions of the Mn-Al-Ti alloys determined via EBSD. Phase wt.% fractions do not sum to 100 % due to a small number of unindexable patterns.

EBSD Property	$Mn_{54}Al_{46}$	$Mn_{53}Al_{46}Ti_1$	$Mn_{54}Al_{45}Ti_1$
True Twin	0.27 ± 0.02	0.45 ± 0.07	0.65 ± 0.03
Order Twin	0.06 ± 0.01	0.09 ± 0.03	0.09 ± 0.02
Pseudo Twin	0.02	0.00	0.00
Grain Area (μm$^{2)}$	29.4	65.3	97.3
Equivalent circle grain diameter (μm)	6.1	9.1	11.1
τ phase wt.%	97.8 ± 3.0	93.8 ± 0.7	98.4 ± 0.6
γ_2 phase wt.%	0 ± 0	2.7 ± 0.6	0.1 ± 0.05

The alloys' magnetic properties were also measured at different temperatures using the VSM. The results are plotted in Fig. 13. VSM hysteresis curves were collected at 25 °C-200 °C at 50 °C intervals. Each sample was kept in the same orientation to the applied field but not demagnetization corrected. Therefore, effects from texture and shape demagnetization may be present in $(BH)_{\max}$, M_r, and $M_{796kA/m}$, and should be understood in terms of their relative change with temperature rather than in their absolute values. Note: because the τ phase does not saturate at the maximum field possible in the VSM used in this study, 796 kA/m, the $M_{796kA/m}$ value is given to represent the magnetic moment at this field but not the true M_s.

4.5. *Thermal stability*

Given the significant changes in phase transformation thermodynamics and kinetics observed via DSC, stability studies were performed to determine if the addition of 1 at.% improved the thermal stability of the τ phase. The as-transformed τ phase samples of each composition were held at 250 °C for up 40 days and held at 550 °C for up to 176 h (~1 week). Samples were tested in the same orientation to the applied field in the VSM but not demagnetization corrected. Fig. 14 shows the evolution of magnetic properties when held at 250 °C and Fig. 15 shows the evolution of magnetic properties when held at 550 °C.

5. Discussion

5.1. *Ab-initio modeling*

The two criteria for choosing ternary elements were as follows: a) does the ternary element segregate to the APB compared to the bulk, and b) does the ternary element favor the FM configuration over the AFM configuration. The results for 12 candidate elements are shown in Figs. 4 and 5. The 12 elements were chosen based on either their known behavior as ternary alloyants in the Mn-Al or Mn-based magnetic systems or based on their low raw material cost of less than 10 USD/kg [1, 47].

As shown in Fig. 5, multiple elements made the FM configuration more stable compared to Mn, as desired. Given the limitations of this model (finite supercell size, Mn-rich composition compared to experiment, and simplified geometry of the APB) the relative difference in APB energy does not necessarily need to be greater than zero for the AFM versus FM nature of the APB to be affected in a real material. Any meaningful effects had to be validated through experiment. Therefore, the candidate elements from these calculations that met both criteria to segregate to the APB and make FM more stable were: Bi, Cr, Ge, Ti, Sn, V, Zn, and Zr. Of these elements, Ti and Sn were chosen for experiment due to their lack of previous study as a ternary alloyant in Mn-based magnets

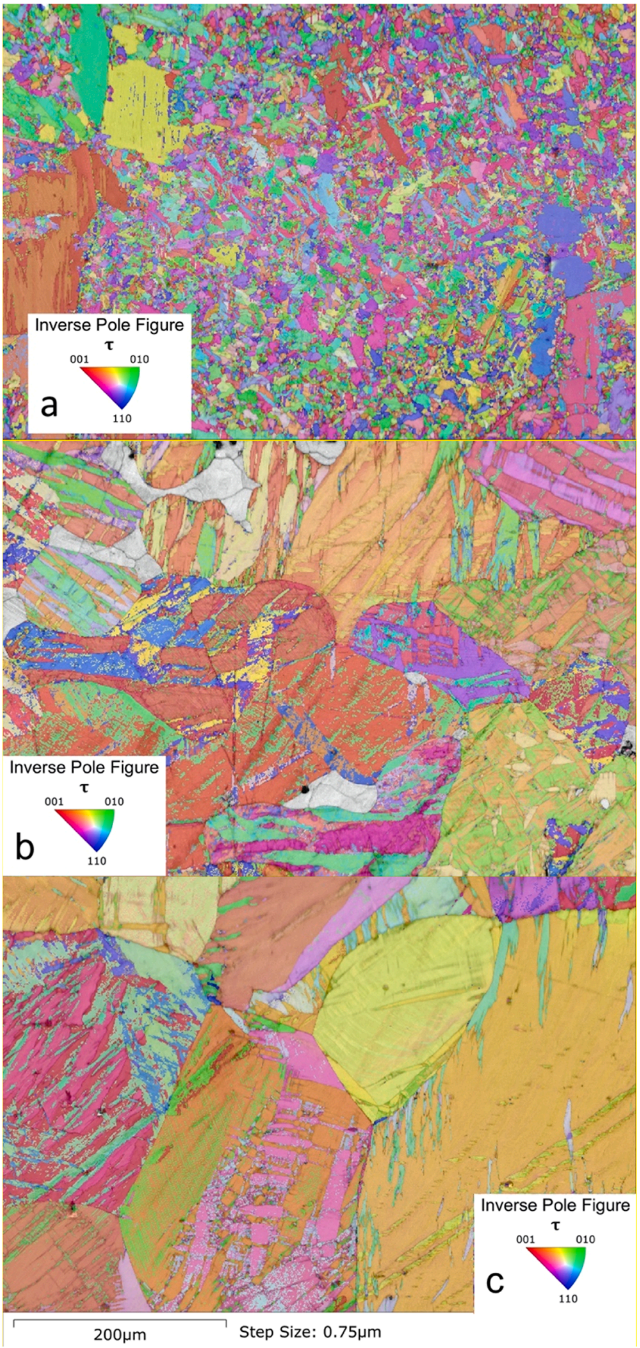

Fig. 9. EBSD τ phase inverse pole figures (IPF) for (a) $Mn_{54}Al_{46}$, (b) $Mn_{53}Al_{46}Ti_1$, and (c) $Mn_{54}Al_{45}Ti_1$. Note the large increase in grain size and twinning of the samples with Ti.

and due to their relatively low raw material cost. Preliminary magnetic studies of the τ phase for 1 at.% Sn and 2 at.% Ti did not show any improvement over $Mn_{54}Al_{46}$, therefore this study was focused on 1 at.% Ti addition.

5.2. Phase transformation

The most notable change in the phase transformation behavior with the addition of 1 at.% Ti is the increase of the τ phase transformation peak by 39–56 °C in Fig. 13. Furthermore, the activation energy values in Table 5 demonstrate that the addition of 1 at.% Ti lowers the activation energy, E_a, barrier for ε' phase ordering and raises the activation energy barrier to transform to the τ phase compared to the base alloy. This is a significant intrinsic effect, because the ordering of ε to ε' is a prerequisite for the displacive mode of the hybrid displacive-diffusional transformation to τ [8]. The ε phase ordering into ε' is visible as a low temperature exotherm in Fig. 13, in agreement with previous results [34,48]. The ordering is followed by displacive shearing to τ that has been shown to result in twinning of the resulting τ phase as a method of stress relaxation [6,7,9,49]. The resulting morphology of this transformation mode is characterized by a plate-like τ phase with a high density of twins and stacking faults. This is in contrast to the diffusional mode, which generally dominates at higher temperatures (>450 °C) and follows a compositionally-invariant massive mode of transformation [5]. While twins have been reported in τ phase grains transformed at higher temperatures where the diffusional massive mechanism dominates, they are not a required feature of the transformation to the same extent as the martensitic displacive mode. To corroborate this, a sample of $Mn_{54}Al_{46}$ ε phase was annealed at 350 °C for 13 h to transform it to the τ phase in a previous study [34]. This temperature is above the temperature of ordering to ε' phase but below the peak transformation temperature to τ phase. After transforming to the τ phase, the relative true twin density was calculated by EBSD to be 0.35, greater than $Mn_{54}Al_{46}$ heat treated at 450 °C (0.27) in this study. Therefore Mn-Al samples transformed at a temperature where the displacive mode is more dominant have a higher twin density, as expected.

Because such a high true twin density was observed with Ti addition, and the source of twinning is as a byproduct of the phase transformation to the τ phase, it follows that the lowering of the E_a barrier for ε' ordering favors the displacive phase transformation pathway, even at 550 °C. The peak of the τ phase transformation was also increased ~40–50 °C with 1 at.% Ti addition. This is an expected result of the increase in E_a for the transformation to τ phase. The overall narrative displayed by this data suggests that the diffusional mode of the transformation from ε to τ is indeed inhibited relative to the displacive mode by the addition of 1 at.% Ti and this, consequently, increases the twin density. More to this point, a small exotherm is visible in Fig. 13 in the 1 at.% Ti alloys near 400 °C, followed by a larger exotherm near 500 °C. In $Mn_{54}Al_{46}$, both the displacive and diffusional transformation modes are active within one τ phase transformation peak near 450 °C, whereas in the alloys with 1 at.% Ti the peaks appear to be split into two, one for each of the two transformation modes. This further suggests that the massive diffusional mode is shifted to higher temperatures as a result of adding 1 at.% Ti. More detailed studies, such as *in-situ* TEM, are needed to confirm this theory.

The implications of raising the phase transformation peak temperature for the τ phase with 1 at.% Ti addition is that the transformation can be performed at higher temperature for longer time periods. This opens up the processing window for conventional techniques such as sintering, meaning that the sintering step could conceivably be combined with the phase transformation to τ phase, simplifying manufacturing.

5.3. Microstructure

The APB density was observed to be significantly decreased in the samples with 1 at.% Ti, as shown in Fig. 8. In fact, the trend in M_r shown in Table 5 from lower to higher between $Mn_{54}Al_{46}$, $Mn_{53}Al_{46}Ti_1$, and $Mn_{54}Al_{45}Ti_1$ matches the trend of decreasing APB density. APBs were only found in twinned grains in this study. It is possible that they were present in non-twinned grains but a thorough search did not observe any APBs outside of twinned regions, which are visible as long striations behind APBs in the TEM BF images [5].

Given that the number of twinned grains in the samples with 1 at.% Ti addition was far greater than without Ti, it could be expected that overall, more APBs would be present in the Ti-alloyed samples – assuming that APBs are indeed only found in the presence of twins. Thus, magnetic performance should suffer. However, once again, recall from DFT that Ti is expected to segregate to the APB and clearly lowers

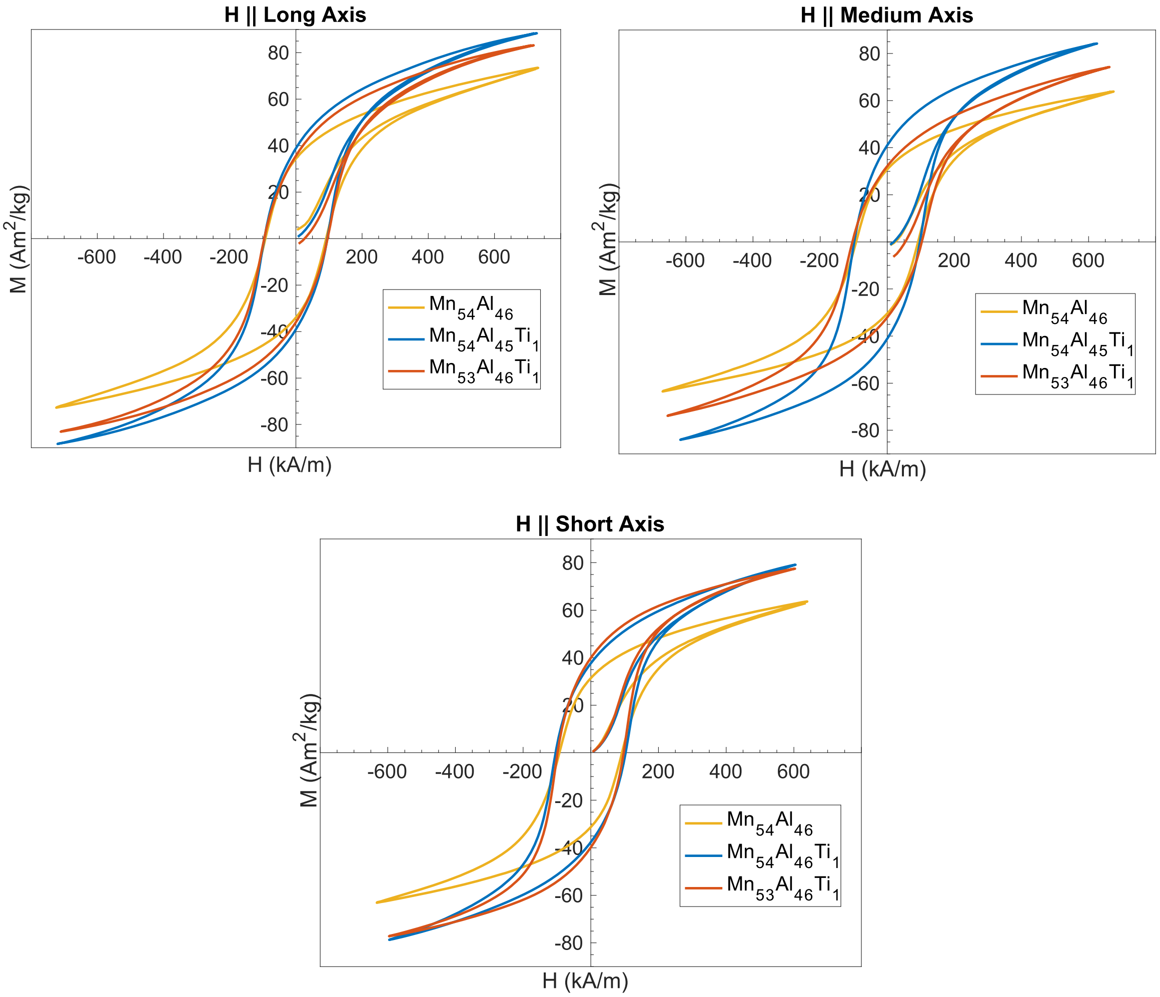

Fig. 10. Demagnetization-corrected VSM curves of the Mn-Al-Ti alloys measured in the three orientations of the rectangular prism samples to observe any effects due to crystal texture.

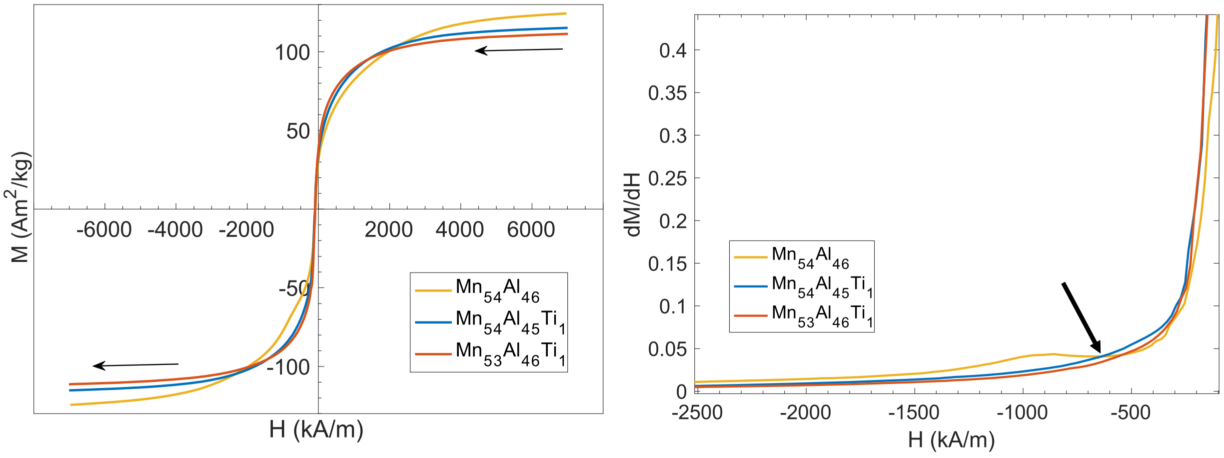

Fig. 11. The high-field VSM M-H and dM/dH reversal curves for the Mn-Al-Ti alloys. The arrows indicate the reversal direction from high positive field to high negative field. The dM/dH data shows the crossover-point in differential χ from the alloys with Ti addition to the $Mn_{54}Al_{46}$ alloy at −600 kA/m.

APB density within twinned grains. Because M_r and H_{ci} were improved with the Ti addition, this implies that the positive benefits of Ti addition on the APB outweigh any negative impacts from increasing twin density. Recall that the negative aspects of APBs are derived from their behavior as AFM-coupled defects and as reverse domain nucleation sites.

In the first case, where APBs are AFM-coupled defects, the addition of Ti may indeed flip the APB configuration from AFM to FM. Thus, the presence of APBs becomes less detrimental because they can contribute to FM behavior. Therefore, because APBs are still present in the Mn-Al-Ti alloys yet cause less AFM behavior in the VSM and thermal VSM data, it is likely that a significant fraction of the APBs take on an FM coupling across the interface in the presence of Ti.

Table 5
The average magnetic properties of the Mn-Al-Ti alloys measured via VSM and their phase transformation peak temperatures measured via DSC.

Alloy	$Mn_{54}Al_{46}$	$Mn_{53}Al_{46}Ti_1$	$Mn_{54}Al_{45}Ti_1$
M_s (Am^2/kg) (at 7162 kA/m)	124	112	115
H_{ci} (kA/m)	92	99	99
$(BH)_{max}$ (kJ/m^3)	4.2	4.9	5.6
M_r (Am^2/kg)	32	36	39
T_C (°C)	375	365	373

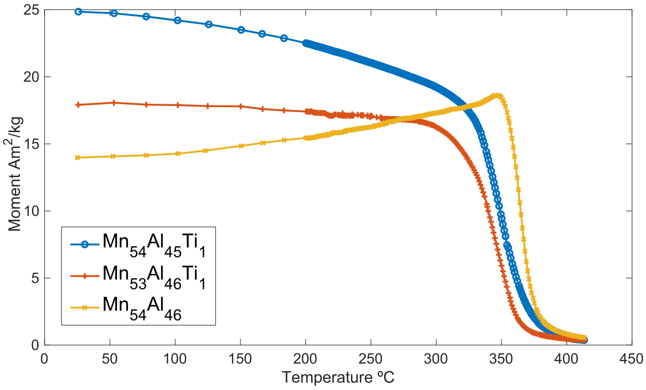

Fig. 12. Magnetic moment of Mn-Al-Ti alloys as a function of temperature. Note the small variation in T_C as well as the AFM behavior shown in $Mn_{54}Al_{46}$ of increasing M with T.

In the second case, by lowering the density of APBs, the density of reversal nucleation sites is lowered. This is significant, because the farther apart nucleation sites are spread, the larger the reversing domains must grow to reverse the entire volume. If the domains must grow larger between nucleation sites, then they are more likely to encounter defects, like dislocations, stacking faults, and twins, all of which can pin the domain walls to slow reversal and improve H_{ci}. Referencing the few studies that have observed both APBs and twins in Mn-Al, the same conclusion can be drawn: twins are more likely to act as pinning sites and APBs are more likely to act as nucleation sites for reversing domains [26,27].

The secondary impacts of adding 1 at.% Ti is an increased density of true twins (76° misorientation) and increased presence of secondary phases γ_2 and β. As stated in the Introduction, previous theories in the literature suggest that these factors should act to diminish H_{ci} and M_r. However, while the negative effects of secondary phases are well established, the effects of twins are less well established. The highly-twinned microstructure is clearly visible when comparing the alloys with and without 1 at.% Ti addition in Fig. 9. The twinned regions are visible as long striations growing out from the grain boundaries, a morphology that agrees with previous EBSD studies on Mn-Al [22,24,25]. While the twinned grains are distributed homogeneously throughout the Mn-Al-Ti alloys, only a few large grains containing a high density of twins are visible in Fig. 9a, surrounded by a majority of small randomly-oriented grains which contain a low density of twins. By contrast, the Mn-Al-Ti samples in Fig. 9b and 9c consist of larger grains intersected by a high density of twins and very few small individual grains. Because neither H_{ci} nor M_r were diminished in the VSM data, the high density of twins does not appear to negatively affect these properties in Mn-Al-Ti alloys.

5.4. Magnetic properties

The VSM curves in Fig. 6 show that the susceptibility, $\chi = M/H$, and M_r are significantly improved for the alloys with Ti addition at low fields in each direction measured. This is despite the fact that at higher fields the M_s of the $Mn_{54}Al_{46}$ alloy is ~10 % greater than with the Ti addition, as shown in the high-field VSM measurement shown in Fig. 7. Were this due to anisotropy of crystal texture or grain shape in the samples with Ti

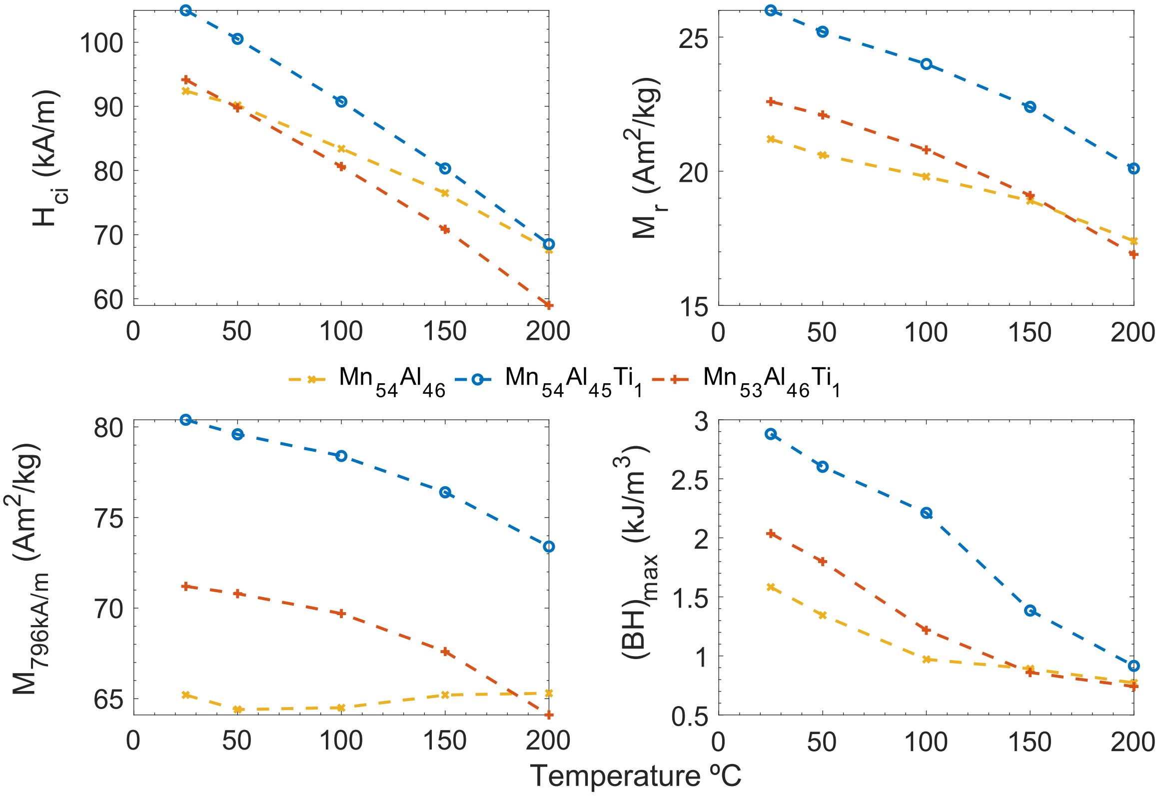

Fig. 13. The VSM curves measured from 25 °C-200 °C show the temperature dependence of the magnetic properties.

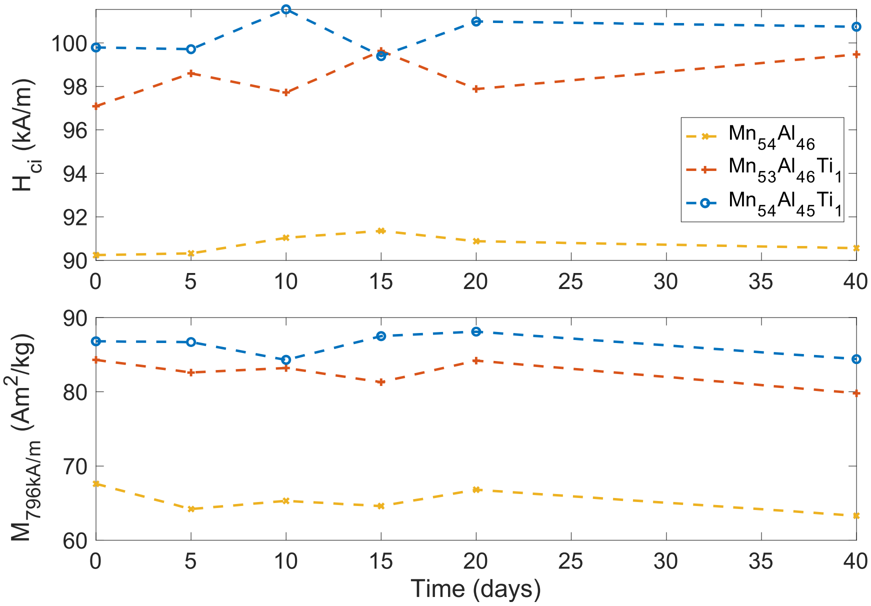

Fig. 14. H_{ci} and $M_{796kA/m}$ as a function of time at 250 °C in air. Samples were not demagnetization corrected so $M_{796kA/m}$ values are relative and not absolute.

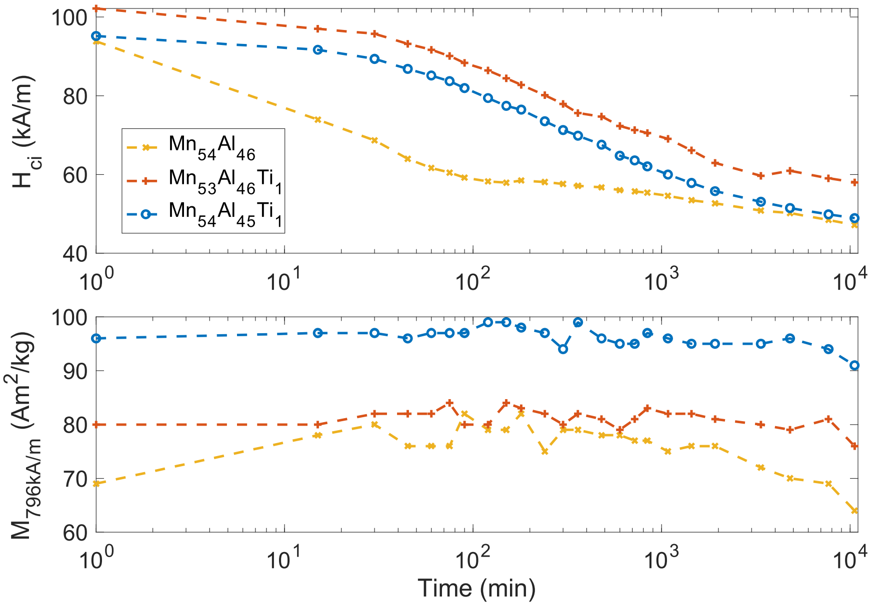

Fig. 15. H_{ci} and $M_{796kA/m}$ as a function of (log) time at 550 °C in air. Samples were not demagnetization corrected so $M_{796kA/m}$ values are relative and not absolute.

addition, then the effect would be pronounced in one direction but would not be in all three. Another mechanism besides anisotropy must be responsible for the improvement. Taking the derivative form of susceptibility yields $d\chi = dM/dH$, allowing the non-linear relationship between M and H to be observed in this material. Clearly, the differential susceptibility of the alloys with 1 at.% Ti is greater at low fields up to 600 kA/m, where the $Mn_{54}Al_{46}$ alloy's reversal behavior changes. There is not only a crossover in the $d\chi$ curves where $Mn_{54}Al_{46}$ becomes the highest $d\chi$, but at this point there is also a noticeable kink in the M-H curve. Sudden, non-linear, increases in M with increasing H have been observed as evidence of metamagnetism in highly-ordered $Mn_{50}Al_{50}$ as a result of AFM ordering [17,18]. In other words, if there is a significant fraction of the τ phase that is taking on an AFM configuration, then it can become evident as a spin-flop from AFM to FM when a sufficiently high field is applied to overcome the crystalline anisotropy of the AFM configuration [50].

As stated previously, DFT modeling demonstrated that APBs prefer the AFM configuration to the FM configuration. Therefore, if there is a sufficiently high density of APBs then the transition from AFM to FM at high fields will be noticeable in VSM measurements, and the superposition of the AFM reversal on top of the FM reversal will appear as a sudden increase in dM/dH, or a kink in the M-H curve. Similar to high-fields, high-temperatures should flip AFM behavior to paramagnetic above the Néel temperature via thermal perturbation.

The magnetic moment of the Mn-Al-Ti alloys with increasing temperature is shown in Fig. 12. As is typical of FM materials, the 1 at.% Ti alloys have a negative trend of M with increasing T up to T_C. As the temperature approaches T_C, there is a dramatic loss of M as a consequence of the transition from FM to paramagnetic. In contrast, $Mn_{54}Al_{46}$ has an increase in M up to near T_C. This again suggests a significant amount of AFM behavior within the $Mn_{54}Al_{46}$ sample. As stated in the Introduction, increasing M with temperature is a previously documented phenomenon in Mn-Al but it has not been the subject of in-depth inquiry. The positive trend of *M* with *T* is indicative of incomplete AFM Néel-type behavior superposed upon the majority FM τ phase Curie behavior. This sums to behavior similar to that observed in certain ferrimagnets such as NiO•Cr_2O_3, as shown in Fig. 16 [51]. This is possible when the *M* of the FM phase decreases less with temperature than the -*M* of the AFM fraction (the APBs). It is worth noting that the slope of the $Mn_{53}Al_{46}Ti_1$ alloy is negative but nearly flat up to 300 °C, somewhere between the positive slope of $Mn_{54}Al_{46}$ and the more negative slope of $Mn_{54}Al_{45}Ti_1$. As was shown in Fig. 8, the density of APBs in $Mn_{53}Al_{46}Ti_1$ lies in between the other two alloys. Therefore, the slope of *M* with increasing *T* is evidently more negative with lower APB density. In other words, the $Mn_{54}Al_{46}$ has the highest APB density and shows the most AFM behavior, $Mn_{54}Al_{45}Ti_1$ has the lowest APB density and shows no clear AFM behavior, and $Mn_{53}Al_{46}Ti_1$ has an APB density in between these two with only a subtle apparent AFM behavior in the *M-T* plot.

Recall that the T_N of AFM Mn-Al is reported to be ~300 °C for $Mn_{50}Al_{50}$, ~75 °C less than the T_C for the FM τ phase [17]. However, given that the *M* continues to increase up to ~350 °C in the $Mn_{54}Al_{46}$ curve, it appears that the T_N of this composition is higher. This could be a compositional effect, where T_N changes with Mn content, or a result of stabilization of spin within AFM domains by the FM τ phase. Considering the case where the AFM behavior arises from APBs within the FM τ phase, which are only one atom thick, it is plausible that the exchange between the FM phase and the AFM defect region becomes exchange-coupled so that the FM phase stabilizes the spin configuration of the AFM APB region and increases T_N [50].

Considering Fig. 13, unlike the Mn-Al-Ti alloys, the $M_{796kA/m}$ of $Mn_{54}Al_{46}$ increases with temperature. This is further evidence of AFM behavior in the alloy without Ti, where instead of thermal perturbations reducing *M* following an FM Curie behavior trend the thermal perturbations increase *M* due an AFM Néel effect flipping atom spins from AFM to paramagnetic. By contrast, the M_r of $Mn_{54}Al_{46}$ does not decrease with temperature. Since M_r is measured at zero applied field, $H = 0$, there is no contribution from any paramagnetic fraction. Therefore, if the AFM fraction in $Mn_{54}Al_{46}$ is made partially paramagnetic as the temperature moves closer to T_N, then it logically follows that the paramagnetic fraction offsets *M* losses to the FM fraction at elevated temperatures and fields ($H = 796$ kA/m), increasing $M_{796kA/M}$ overall. In theory, the paramagnetic AFM fraction does nothing to increase M_r at $H = 0$ since there is no applied field, in good agreement with the evidence.

Based on the combined results from the high-field VSM and the thermal VSM, there is clear evidence of AFM behavior in $Mn_{54}Al_{46}$ in addition to the expected FM behavior of the τ phase. Therefore, given the microstructural evidence of lowered APB density with Ti addition and the lack of AFM behavior in the Mn-Al-Ti alloys, the APBs are the most likely source of the AFM behavior and suppressing their formation has a positive impact on the magnetic properties.

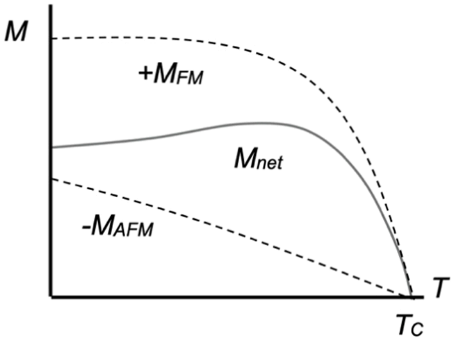

Fig. 16. Schematic of magnetic moment varying with temperature for a NiO•Cr_2O_3 ferrimagnet where the superposition of AFM moment behavior and FM moment behavior results in a similar curve to that observed in $Mn_{54}Al_{46}$. Redrawn from [51].

5.5. *Thermal stability*

To better understand the data in Fig. 13, the thermal coefficients of M_r and H_{ci} were calculated using a linear least-squares best-fit for each alloy. M_r coefficients of −0.10%/ °C, −0.13%/ °C, and −0.14 %/ °C were measured for $Mn_{54}Al_{46}$, $Mn_{54}Al_{45}Ti_1$, and $Mn_{53}Al_{46}Ti_1$, respectively. The M_r coefficient for Sm-Co is ~−0.035%/ °C and for Nd-Fe-B is ~−0.1 %/ °C [52]. H_{ci} coefficients of −0.15%/ °C, −0.20%/ °C, and −0.21 %/ °C were measured for $Mn_{54}Al_{46}$, $Mn_{54}Al_{45}Ti_1$, and $Mn_{53}Al_{46}Ti_1$, respectively. These are all roughly one-third the negative thermal coefficient of H_{ci} for Nd-Fe-B (−0.6%/ °C), and as good if not slightly better than Sm-Co at −0.2%/ °C to −0.31%/ °C, depending on the composition. This is important because due to these trends, $(BH)_{max}$ for Nd-Fe-B PMs drops off sharply at elevated temperatures, losing ~80 % of room temperature performance at 200 °C, which limits its performance range [53]. By contrast, 49 %, 32 %, and 36 % of room temperature $(BH)_{max}$ was maintained at 200 °C for $Mn_{54}Al_{46}$, $Mn_{54}Al_{45}Ti_1$, and $Mn_{53}Al_{46}Ti_1$, respectively.

The magnetic properties of the τ phase in the three alloys were generally stable even up to 40 days at 250 °C, as shown in Fig. 14. The change in $M_{796kA/m}$ from 0 days to 40 days was −6.4 %, −5.3 %, and −2.8 % for $Mn_{54}Al_{46}$, $Mn_{53}Al_{46}Ti_1$, and $Mn_{54}Al_{45}Ti_1$ respectively. The same alloys showed a small increase in H_{ci} after 40 days of 0.4 %, 2.5 %, and 1.0 %. The loss of $M_{796kA/m}$ and gain in H_{ci} is the expected trend for Mn-Al at this temperature based on the metastable nature of the τ phase. The slight loss of $M_{796kA/m}$ in each alloy is most likely due to phase decomposition of the τ phase into the equilibrium γ_2 and β phases. Since these two phases are effective pinning sites to domain wall motion, as they increase in volume there is an associated increase in H_{ci} [15,54]. Given that the alloys with 1 at.% Ti showed a smaller loss of $M_{796kA/m}$ than $Mn_{54}Al_{46}$, the addition of Ti does not appear to destabilize the τ phase and instead is shown to increase phase stability at 250 °C.

More insight into this is shown in the samples annealed at 550 °C for up to 1 week, see Fig. 15. At this higher temperature, the differences between the 1 at.% alloys and the base alloy become more apparent. First, the drop in H_{ci} from 1 min to 15 min in $Mn_{54}Al_{46}$ was dramatic, losing 21 % compared to the Mn-Al-Ti alloys at ~5 %. Only after 120 min did the slope of H_{ci} for $Mn_{54}Al_{46}$ level off. The Mn-Al-Ti alloys, by comparison, have a minimal drop in H_{ci} until 90 min, at which point their curves approach the same slope as the initial slope in $Mn_{54}Al_{46}$. Bearing in mind that the 1 at.% alloys had already been annealed for 1 h at 550 °C, the addition of Ti significantly improved the stability of H_{ci} at 550 °C. The $M_{796kA/m}$ values were largely constant for the 1 at.% alloys, dropping by only ~5 % from 1 min to 10^4 min. There was some variation in the $M_{796kA/m}$, which was to be expected since this temperature is where the transformation to the τ phase occurs and additional ordering of the $L1_0$ structure is likely, which improves $M_{796kA/m}$. Taking the difference from the maximum $M_{796kA/m}$ value to the value at 10^4 min gave a drop of no more than 10 % for both $Mn_{53}Al_{46}Ti_1$ and $Mn_{54}Al_{45}Ti_1$. By comparison, the drop in $M_{796kA/m}$ for $Mn_{54}Al_{46}$ was more complex and dramatic. Despite being ~98 wt.% τ phase by both XRD and EBSD measurements, $M_{796kA/m}$ increased by 14 % after 30 min. It then dropped from this maximum by 18 % after 10^4 min, with an overall drop from 1 min to 10^4 min of 7 %.

The addition of 1 at.% evidently improved the stability of H_{ci} and $M_{796kA/m}$ at 550 °C but the mechanism is not obviously clear. The crystalline anisotropy contribution to H_{ci} is an intrinsic property of the τ phase and should not change when held at constant temperature. The microstructural contribution to H_{ci}, however, can change over time as the microstructure evolves. The $Mn_{54}Al_{46}$ sample had the highest APB density and lowest twin density, with roughly the same density of GNDs as with 1 at.% Ti. The samples with 1 at.% Ti had a much higher twin density and lower APB density. APBs and GNDs can move within grains at this temperature and could be annealed out over sufficiently long time spans [55,56]. The loss of APBs and dislocations in favor of a well-ordered $L1_0$ structure explains the gain in $M_{796kA/m}$ observed in the first 30 min at 550 °C. However, the mutual annihilation of dislocations out of the $Mn_{54}Al_{46}$ sample is also an explanation for the dramatic loss of H_{ci}.

Given than dislocations are well documented as a primary mechanism for increasing H_{ci} in Mn-Al by domain wall pinning, one theory is that the addition of 1 at.% Ti inhibits dislocation motion [25,57,58]. For instance, dislocations are impeded when they encounter other dislocations, solute atoms, precipitates, twins, and grain boundaries, as they all interact with the strain field of the dislocation [59]. The addition of Ti as a solute atom therefore likely impeded dislocation motion, but the high density of nanoscale true twins was another useful mechanism to slow dislocation motion. The TEM images in Fig. 12 show twins of <100 nm across. In other alloys, nanotwins have been shown to be as effective as grain boundaries in strengthening via the Hall-Petch mechanism of impeding dislocation motion, but this mechanism has yet to be studied in Mn-Al [60,61]. Thus, despite the generally smaller grain size of the $Mn_{54}Al_{46}$ alloy, the addition of 1 at.% Ti was shown to preserve H_{ci} at 550 °C for significantly longer, most likely by impeding dislocation motion with solute atoms and twins.

Improving the stability of $M_{796kA/m}$ and H_{ci} at elevated temperatures is essential to manufacturing Mn-Al PMs with high $(BH)_{\max}$. This is the reason for the common use of C as an interstitial alloyant in Mn-Al because it stabilizes the τ phase against decomposition without significantly diminishing the magnetic performance [15,62,63]. The conventional processing route for PMs of powder milling, magnetic aligning, and sintering into a bulk shape cannot be optimized if the magnetic properties achieved after milling are lost during sintering [64–66]. Therefore, the addition of 1 at.% Ti widens the temperature and time window in which sintering can be performed, opening the door for new processing routes.

6. Conclusions

Ab-initio calculations demonstrated that Ti segregates to APB defects in the FM τ phase and motivates FM coupling across the APB compared to AFM coupling in the reference case. This is significant because APBs are a byproduct of the displacive-diffusional phase transformation from the ε phase to the τ phase. APBs result in AFM-coupling between Mn atoms across the boundary. Such AFM behavior was observed in the VSM data for the Mn-Al alloy but not for the Mn-Al-Ti alloys. TEM showed that the addition of Ti lowered the APB density when substituted for Al or for Mn in $Mn_{54}Al_{46}$. The frequency of true twin defects increased with 1 at.% Ti addition, but the only negative effect was a small loss of M_s. Order twin density was low and relatively unchanged by the Ti addition. The increase in twin density was attributed partially to changes in the hybrid displacive-diffusional phase transformation, suggesting that the addition of 1 at.% Ti favors the displacive mode. In part by suppressing APBs, M_r and H_{ci} were improved in the Mn-Al-Ti alloys despite the high density of true twins. Notably, APBs were only observed within twinned regions, indicating that the presence of twins in Mn-Al is usually accompanied by APBs. Therefore, the twins themselves may not be the source of negative magnetic effects observed in previous studies. Rather, APBs within the twinned regions may be the primary contributor to loss of M_r and H_{ci} in the τ phase, and have been overlooked as a root cause. The Mn-Al-Ti alloys had significantly better stability of H_{ci} and $M_{796kA/m}$ when held at 550 °C, showing that the addition of 1 at.% improves τ phase stability and slows the loss of microstructural defects that improve H_{ci}.

Declaration of Competing Interest

The authors declare that they have no known competing financial interests or personal relationships that could have appeared to influence the work reported in this paper.

Acknowledgements

This work was supported by the National Science Foundation under awards 1852529 and 2032592. This work also includes high-field VSM data acquired at the Ames National Laboratory, which is operated for the US Department of Energy by Iowa State University under contract DE-AC02-07CH11358. Special thanks to Dr. Jun Cui and Dr. Wei Tang for their assistance.

References

[1] T. Keller, I. Baker, Manganese-based permanent magnet materials, Prog. Mater Sci. 124 (2022) 100872, https://doi.org/10.1016/j.pmatsci.2021.100872.

[2] V. Øygarden, J. Rial, A. Bollero, S. Deledda, Phase-pure τ-MnAlC produced by mechanical alloying and a one-step annealing route, J. Alloys Compd. 779 (2019) 776–783, https://doi.org/10.1016/j.jallcom.2018.11.175.

[3] H. Fang, J. Cedervall, F.J.M. Casado, Z. Matej, J. Bednarcik, J. Ångström, P. Berastegui, M. Sahlberg, Insights into formation and stability of τ-$MnAlZ_x$ (Z = C and B), J. Alloys Compd. 692 (2017) 198–203, https://doi.org/10.1016/j.jallcom.2016.09.047.

[4] J.M.K. Wiezorek, A.K. Kulovits, C. Yanar, W.A. Soffa, Grain boundary mediated displacive-diffusional formation of τ-phase MnAl, Metall. Mater. Trans. A Phys. Metall. Mater. Sci. 42 (2011) 594–604, https://doi.org/10.1007/s11661-010-0308-1.

[5] C. Yanar, J.M.K. Wiezorek, V. Radmilovic, W.A. Soffa, Massive transformation and the formation of the ferromagnetic $L1_0$ phase in manganese-aluminum-based alloys, Metall. Mater. Trans. A Phys. Metall. Mater. Sci. 33 (2002) 2413–2423, https://doi.org/10.1007/s11661-002-0363-3.

[6] S. Kojima, T. Ohtani, N. Kato, K. Kojima, Y. Sakamoto, I. Konno, M. Tsukahara, T. Kubo, Crystal transformation and orientation of Mn-Al-C hard magnetic alloy, 768 (2008) 768–769. 10.1063/1.30281.

[7] A.S. Sologubenko, P. Müllner, H. Heinrich, G. Kostorz, On the plate-like τ-phase formation in MnAl–C alloys, Z. Metallkd. 95 (2004) 486–491, https://doi.org/10.3139/146.017981.

[8] P. Müllner, B.E. Bürgler, H. Heinrich, A.S. Sologubenko, G. Kostorz, Observation of the shear mode of the ε → τ phase transformation in a Mn-Al-C single crystal, Philos. Mag. Lett. 82 (2002) 71–79, https://doi.org/10.1080/09500830110103225.

[9] A.S. Sologubenko, P. Müllner, H. Heinrich, G. Kostorz, TEM study of the ε→ε′→τ phase transformation in Mn-Al-C alloys, Microsc. Microanal. 9 (2003) 350–351, https://doi.org/10.1017/s143192760302628x.

[10] A.S. Sologubenko, P. Müllner, H. Heinrich, M. Woligarten, G. Kostorz, The effect of composition and stress on the selection of epsilon to tau transformation modes in MnAl-C, J. Phys. IV 112 (2003) 1071–1074.

[11] S. Arapan, P. Nieves, S. Cuesta-López, M. Gusenbauer, H. Oezelt, T. Schrefl, E. K. Delczeg-Czirjak, H.C. Herper, O. Eriksson, Influence of antiphase boundary of the MnAl τ -phase on the energy product, Phys. Rev. Mater. 3 (2019) 1–5, https://doi.org/10.1103/PhysRevMaterials.3.064412.

[12] S. Bance, F. Bittner, T.G. Woodcock, L. Schultz, T. Schrefl, Role of twin and anti-phase defects in MnAl permanent magnets, Acta Mater. 131 (2017) 48–56, https://doi.org/10.1016/j.actamat.2017.04.004.

[13] H. Zijlstra, Coping with Brown's paradox: the pinning and nucleation of magnetic domain walls at antiphase boundaries, IEEE Trans. Magn. 15 (1979) 1246–1250, https://doi.org/10.1109/TMAG.1979.1060313.

[14] H. Zijlstra, H.B. Haanstra, Evidence by Lorentz microscopy for magnetically active stacking faults in MnAl alloy, J. Appl. Phys. 37 (1966) 2853–2856, https://doi.org/10.1063/1.1782138.

[15] Q. Zeng, I. Baker, J.B. Cui, Z.C. Yan, Structural and magnetic properties of nanostructured Mn-Al-C magnetic materials, J. Magn. Magn. Mater. 308 (2007) 214–226, https://doi.org/10.1016/j.jmmm.2006.05.032.

[16] N. Singh, V. Mudgil, K. Anand, A.K. Srivastava, R.K. Kotnala, A. Dhar, Influence of processing on structure property correlations in τ-MnAl rare-earth free permanent magnet material, J. Alloys Compd. 633 (2015) 401–407, https://doi.org/10.1016/j.jallcom.2015.02.041.

[17] S. Sato, S. Irie, Y. Nagamine, T. Miyazaki, Y. Umeda, Antiferromagnetism in perfectly ordered $L1_0$-MnAl with stoichiometric composition and its mechanism, Sci. Rep. 10 (2020) 1–10, https://doi.org/10.1038/s41598-020-69538-2.

[18] S. Sato, S. Irie, Metamagnetic behavior in L10-MnAl synthesized by the post annealing of electrodeposited MnAl powder, AIP Adv. 9 (2019), https://doi.org/10.1063/1.5079929.

[19] S. Mican, D. Benea, R. Hirian, R. Gavrea, O. Isnard, V. Pop, M. Coldea, Structural, electronic and magnetic properties of the $Mn_{50}Al_{46}Ni_4$ alloy, J. Magn. Magn. Mater. 401 (2016) 841–847, https://doi.org/10.1016/j.jmmm.2015.11.011.

[20] A.D. Crisan, F. Vasiliu, R. Nicula, C. Bartha, I. Mercioniu, O. Crisan, Thermodynamic, structural and magnetic studies of phase transformations in MnAl nanocomposite alloys, Mater. Charact. 140 (2018) 1–8, https://doi.org/10.1016/j.matchar.2018.03.034.

[21] F. Jiménez-Villacorta, J.L. Marion, J.T. Oldham, M. Daniil, M.A. Willard, L. H. Lewis, Magnetism-structure correlations during the ε→τ transformation in Rapidly-Solidified mnal nanostructured alloys, Metals 4 (2014) 8–19, https://doi.org/10.3390/met4010008 (Basel).

[22] Y. Jia, H. Ding, Y. Wu, J. Wang, H. Wu, T. Ma, S. Zhao, K.P. Skokov, A. Aubert, F. Maccari, O. Gutfleisch, Y. Xu, J. Niu, B. Qiao, S. Zhao, C. Jiang, On the ε → τ

phase transformation and twinning in L10−MnAl alloys, Acta Mater. 232 (2022) 117892, https://doi.org/10.1016/j.actamat.2022.117892.

[23] J. Thielsch, F. Bittner, T.G. Woodcock, Magnetization reversal processes in hot-extruded τ-MnAl-C, J. Magn. Magn. Mater. 426 (2017) 25–31, https://doi.org/10.1016/j.jmmm.2016.11.045.

[24] F. Bittner, L. Schultz, T.G. Woodcock, Twin-like defects in L1$_0$ ordered τ-MnAl-C studied by EBSD, Acta Mater. 101 (2015) 48–54, https://doi.org/10.1016/j.actamat.2015.08.044.

[25] Y. Jia, Y. Wu, S. Zhao, S. Zuo, K.P. Skokov, O. Gutfleisch, C. Jiang, H. Xu, L1$_0$ rare-earth-free permanent magnets: the effects of twinning versus dislocations in Mn-Al magnets, Phys. Rev. Mater. 4 (2020) 1–17, https://doi.org/10.1103/PhysRevMaterials.4.094402.

[26] J.V. Landuyt, G.V. Tendeloo, J.J.V.D. Broek, H. Donkersloot, H. Zijlstra, Defect structure and magnetic properties of MnAI permanent magnet materials, IEEE Trans. Magn. 14 (1978) 679–681, https://doi.org/10.1109/TMAG.1978.1059949.

[27] J.P. Jakubovics, A.J. Lapworth, T.W. Jolly, Electron microscope studies of ferromagnetic ordered structures, J. Appl. Phys. 49 (1978) 2002–2006, https://doi.org/10.1063/1.324777.

[28] E.L. Houseman, J.P. Jakubovics, Domain structure and magnetization processes in MnAl and MnAlC alloys, J. Magn. Magn. Mater. 31–34 (1983) 1005–1006, https://doi.org/10.1016/0304-8853(83)90770-9.

[29] S.F. Marenkin, A.I. Ril', Al–Mn hard magnetic alloys as promising materials for permanent magnets (Review), Russ. J. Inorg. Chem. 65 (2020) 2007–2019, https://doi.org/10.1134/s003602362014003x.

[30] T. Mix, T.G. Woodcock, Advanced thermal stability investigations of the Mn–Al-Ga system, Results Mater. 5 (2020) 100068, https://doi.org/10.1016/j.rinma.2020.100068.

[31] T. Keller, W. Yang, W. Chen, I. Baker, Additive manufacturing of Mn-Al permanent magnets via laser powder bed fusion, Materialia 33 (2024) 101978, https://doi.org/10.1016/j.mtla.2023.101978 (Oxf).

[32] R. Gavrea, R. Hirian, S. Mican, D. Benea, O. Isnard, M. Coldea, V. Pop, Structural, electronic and magnetic properties of the Mn54−xAl46Tix (x = 2; 4) alloys, Intermetallics 82 (2017) 101–106, https://doi.org/10.1016/j.intermet.2016.11.012 (Barking).

[33] A. Aharoni, Demagnetizing factors for rectangular ferromagnetic prisms, J. Appl. Phys. 83 (1998) 3432–3434, https://doi.org/10.1063/1.367113.

[34] T. Keller, D. Barbagallo, N. Sheremetyeva, T.K. Ghosh, K.S. Shanks, G. Hautier, I. Baker, The phase transformation behavior of Mn-Al rare-earth-free permanent magnets, J. Magn. Magn. Mater. 587 (2023) 171331, https://doi.org/10.1016/j.jmmm.2023.171331.

[35] G. Kresse, D. Joubert, From ultrasoft pseudopotentials to the projector augmented-wave method, Phys. Rev. B 59 (1999) 1758–1775, https://doi.org/10.1103/PhysRevB.59.1758.

[36] G. Kresse, J. Furthmüller, Efficient iterative schemes for ab initio total-energy calculations using a plane-wave basis set, Phys. Rev. B 54 (1996) 11169–11186, https://doi.org/10.1103/PhysRevB.54.11169.

[37] G. Kresse, J. Furthmüller, Efficiency of ab-initio total energy calculations for metals and semiconductors using a plane-wave basis set, Comput. Mater. Sci. 6 (1996) 15–50, https://doi.org/10.1016/0927-0256(96)00008-0.

[38] G. Kresse, J. Hafner, Ab initio molecular dynamics for liquid metals, Phys. Rev. B 47 (1993) 558–561.

[39] P. Nieves, S. Arapan, T. Schrefl, S. Cuesta-Lopez, Atomistic spin dynamics simulations of the MnAl τ -phase and its antiphase boundary, Phys. Rev. B 96 (2017) 1–10, https://doi.org/10.1103/PhysRevB.96.224411.

[40] C. Freysoldt, B. Grabowski, T. Hickel, J. Neugebauer, G. Kresse, A. Janotti, C. G. Van De Walle, First-principles calculations for point defects in solids, Rev. Mod. Phys. 86 (2014) 253–305, https://doi.org/10.1103/RevModPhys.86.253.

[41] H.E. Kissinger, Reaction kinetics in differential thermal analysis, Anal. Chem. 29 (1957) 1702–1706. https://pubs.acs.org/sharingguidelines.

[42] T.H. Grgurić, D. Manasijević, S. Kožuh, I. Ivanić, I. Anžel, B. Kosec, M. Bizjak, E. G. Bajsić, L. Balanović, M. Gojić, The effect of the processing parameters on the martensitic transformation of Cu-Al-Mn shape memory alloy, J. Alloys Compd. 765 (2018) 664–676, https://doi.org/10.1016/j.jallcom.2018.06.250.

[43] Y. Chen, Q. Wang, Thermal oxidative degradation kinetics of flame-retarded polypropylene with intumescent flame-retardant master batches *in situ* prepared in twin-screw extruder, Polym. Degrad. Stab. 92 (2007) 280–291, https://doi.org/10.1016/j.polymdegradstab.2006.11.004.

[44] R. Osmundsen, I. Baker, The annihilation of antiphase boundary tubes and their effect on strengthening in Ni3Al, Acta Mater. 237 (2022), https://doi.org/10.1016/j.actamat.2022.118185.

[45] B.D. Cullity, Elements of X-Ray Diffraction, 2nd ed., Addison-Wesley Publishing Co, Reading MA, 1978.

[46] J.Z. Wei, Z.G. Song, Y.C.B.C. Yang, S.Q. Liu, H.L. Du, J.Z. Han, D. Zhou, C.S. Wang, Y.C.B.C. Yang, A. Franz, D. Többens, J.B. Yang, τ-MnAl with high coercivity and saturation magnetization, AIP Adv. 4 (2014), https://doi.org/10.1063/1.4903773.

[47] U.S. Geological Survey, Mineral Commodity Summaries, 2020. 10.3133/mcs2020.

[48] A.M. Genc, O. Acar, S. Turan, I. Kalay, U. Savacı, Y.E. Kalay, Investigation of phase selection hierarchy in Mn–Al alloys, Intermetallics 115 (2019) 106617, https://doi.org/10.1016/j.intermet.2019.106617 (Barking).

[49] C. Zhang, T. Zhang, J. Wang, S. Zhao, Y. Wu, C. Jiang, Anisotropic single-variant of (Mn$_{54}$Al$_{46}$)$_{97}$C$_3$, Scr. Mater. 143 (2018) 72–76, https://doi.org/10.1016/j.scriptamat.2017.09.008.

[50] J.M.D. Coey, Magnetism and Magnetic Materials, Cambridge University Press, 2004.

[51] B.D. Cullity, C.D. Graham, Introduction to Magnetic Materials, 2nd ed., John Wiley and Sons Inc., Piscataway, 2009.

[52] K.H. Müller, S. Sawatzki, R. Gauß, O. Gutfleisch, Permanent magnet materials. Handbook of Magnetism and Magnetic Materials, Springer International Publishing, Cham, 2021, pp. 1–65, https://doi.org/10.1007/978-3-030-63101-7_29-1.

[53] J. Cui, M. Kramer, L. Zhou, F. Liu, A. Gabay, G. Hadjipanayis, B. Balasubramanian, D. Sellmyer, Current progress and future challenges in rare-earth-free permanent magnets, Acta Mater. 158 (2018) 118–137, https://doi.org/10.1016/j.actamat.2018.07.049.

[54] A. Chaturvedi, R. Yaqub, I. Baker, Microstructure and magnetic properties of bulk nanocrystalline MnAl, Metals 4 (2014) 20–27, https://doi.org/10.3390/met4010020 (Basel).

[55] J.S. Gau, R.K. Mishra, G. Thomas, Electron microscopy of Mn-Al-C magnets, IEEE Trans. Magn. 19 (1983) 2256–2260, https://doi.org/10.1109/TMAG.1983.1062798.

[56] D. Hull, D.J. Bacon, Introduction to Dislocations, Butterworth-Heinemann, Oxford, 2011. https://search.ebscohost.com/login.aspx?direct=true&db=e000xna&AN=379941&site=ehost-live&scope=site&authtype=ip,shib&custid=dartcol&group=main.

[57] F. Bittner, J. Freudenberger, L. Schultz, T.G. Woodcock, The impact of dislocations on coercivity in L1$_0$-MnAl, J. Alloys Compd. 704 (2017) 528–536, https://doi.org/10.1016/j.jallcom.2017.02.028.

[58] H. Kronmüller, The contribution of dislocations to the magnetocrystalline energy and their effect on rotational hysteresis processes, J. Appl. Phys. 38 (1967) 1314–1315, https://doi.org/10.1063/1.1709599.

[59] K. Lu, L. Lu, S. Suresh, Strengthening materials by engineering coherent internal boundaries at the nanoscale, Science 324 (2009) 349–352 (1979), https://www.science.org.

[60] L. Lu, R. Schwaiger, Z.W. Shan, M. Dao, K. Lu, S. Suresh, Nano-sized twins induce high rate sensitivity of flow stress in pure copper, Acta Mater. 53 (2005) 2169–2179, https://doi.org/10.1016/j.actamat.2005.01.031.

[61] J.W. Christian, S. Mahajan, Deformation twinning, Prog. Mater. Sci. 39 (1995) 1–157, https://doi.org/10.1016/0079-6425(94)00007-7.

[62] O. Obi, L. Burns, Y. Chen, T. Fitchorov, S. Kim, K. Hsu, D. Heiman, L.H. Lewis, V. G. Harris, Magnetic and structural properties of heat-treated high-moment mechanically alloyed MnAlC powders, J. Alloys Compd. 582 (2014) 598–602, https://doi.org/10.1016/j.jallcom.2013.08.086.

[63] L. Pareti, F. Bolzoni, F. Leccabue, A.E. Ermakov, Magnetic anisotropy of MnAl and MnAlC permanent magnet materials, J. Appl. Phys. 59 (1986) 3824–3828, https://doi.org/10.1063/1.336723.

[64] W. Tang, G. Ouyang, X. Liu, J. Wang, B. Cui, J. Cui, Engineering microstructure to improve coercivity of bulk MnBi magnet, J. Magn. Magn. Mater. 563 (2022), https://doi.org/10.1016/j.jmmm.2022.169912.

[65] M. Tyrman, S. Ahmim, A. Pasko, V. Etgens, F. Mazaleyrat, S. Quetel-Weben, L. Perrière, I. Guillot, Anisotropy of the ferromagnetic L10 phase in the Mn-Al-C alloys induced by high-pressure spark plasma sintering, AIP Adv. 8 (2018) 0–6, https://doi.org/10.1063/1.5007241.

[66] F. Maccari, A. Aubert, S. Ener, E. Bruder, I. Radulov, K. Skokov, O. Gutfleisch, Formation of pure τ -phase in Mn–Al–C by fast annealing using spark plasma sintering, J. Mater. Sci. 57 (2022) 6056–6065, https://doi.org/10.1007/s10853-022-07002-4.